

while children had detectable antibodies to PfSEA-1. These data suggest that anti-PfSEA-1 responses could augment responses to other targets, such as PfEMP-1, that may protect against severe malaria (24). Under conditions of natural exposure, only 6% of 1.5- to 3.5-year-old children in our cohort had detectable antibodies to PfSEA-1. This low natural prevalence suggests that adjuvanted vaccination with PfSEA-1 could have a marked impact on reducing severe malaria in young children.

In a second longitudinal Kenyan cohort, anti-PfSEA-1 antibodies were associated with significant protection against parasitemia in adolescents and young adults. Individuals with detectable IgG anti-rPfSEA-1A antibodies had 50% lower parasite densities over 18 weeks of follow-up compared with individuals with no detectable IgG anti-rPfSEA-1A antibodies. It was noteworthy that the prevalence of detectable anti-rPfSEA-1A antibodies in this age group (56%) was substantially higher than in our birth cohort, which suggests that natural exposure boosts anti-PfSEA-1 antibody levels.

Together, our data validate our field-to-lab-to-field-based strategy for the rational identification of vaccine candidates and support PfSEA-1 as a candidate for pediatric falciparum malaria. By blocking schizont egress, PfSEA-1 may synergize with other vaccines targeting hepatocyte (25) and RBC invasion (26).

REFERENCES AND NOTES

1. C. J. Murray *et al.*, *Lancet* **379**, 413–431 (2012).
2. WHO, *The World Malaria Report* (WHO, Switzerland, 2012); www.who.int/malaria/publications/world_malaria_report_2012/en/index.html.
3. S. Okie, *N. Engl. J. Med.* **353**, 1877–1881 (2005).
4. WHO, Malaria Vaccine Rainbow Tables (2012); www.who.int/vaccine_research/links/Rainbow/en/index.html.
5. A. N. Hodder, P. E. Crewther, R. F. Anders, *Infect. Immun.* **69**, 3286–3294 (2001).
6. A. Sabchareon *et al.*, *Am. J. Trop. Med. Hyg.* **45**, 297–308 (1991).
7. J. D. Kurtis, D. E. Lanar, M. Opollo, P. E. Duffy, *Infect. Immun.* **67**, 3424–3429 (1999).
8. T. K. Mutabingwa *et al.*, *PLOS Med.* **2**, e407 (2005).
9. R. Spaccapelo *et al.*, *Sci. Rep.* **1**, 39 (2011).
10. N. D. Gómez *et al.*, *PLOS ONE* **6**, e25477 (2011).
11. M. Kadepoppala, R. A. O'Donnell, M. Grainger, B. S. Crabb, A. A. Holder, *Eukaryot. Cell* **7**, 2123–2132 (2008).
12. C. P. Nixon *et al.*, *J. Infect. Dis.* **192**, 861–869 (2005).
13. M. Treeck, J. L. Sanders, J. E. Elias, J. C. Boothroyd, *Cell Host Microbe* **10**, 410–419 (2011).
14. M. Manske *et al.*, *Nature* **487**, 375–379 (2012).
15. J. D. Dvorin *et al.*, *Science* **328**, 910–912 (2010).
16. A. Farrell *et al.*, *Science* **335**, 218–221 (2012).
17. M. J. Blackman, H. G. Heidrich, S. Donachie, J. S. McBride, A. A. Holder, *J. Exp. Med.* **172**, 379–382 (1990).
18. E. S. Bergmann-Leitner, E. H. Duncan, E. Angov, *Malar. J.* **8**, 183 (2009).
19. N. Ahlborg *et al.*, *Exp. Parasitol.* **82**, 155–163 (1996).
20. I. D. Goodyer, B. Pouvelle, T. G. Schneider, D. P. Trelka, T. F. Taraschi, *Mol. Biochem. Parasitol.* **87**, 13–28 (1997).
21. S. Yoshida *et al.*, *PLOS ONE* **5**, e13727 (2010).
22. J. D. Kurtis, R. Mitalib, F. K. Onyango, P. E. Duffy, *Infect. Immun.* **69**, 123–128 (2001).
23. J. C. Beier *et al.*, *Am. J. Trop. Med. Hyg.* **50**, 529–536 (1994).
24. P. C. Bull *et al.*, *J. Infect. Dis.* **192**, 1119–1126 (2005).
25. RTS,S Clinical Trials Partnership, *N. Engl. J. Med.* **365**, 1863–1875 (2011).
26. C. Crosnier *et al.*, *Nature* **480**, 534–537 (2011).

ACKNOWLEDGMENTS

The authors thank the Mother Offspring Malaria Study project staff for their efforts in collecting clinical data, processing samples, and interpreting malaria blood smears, as well as the study

participants and their families. Ethical clearance was obtained from the institutional review boards of the Seattle Biomedical Research Institute and Rhode Island Hospital; the Medical Research Coordinating Committee of the National Institute for Medical Research, Tanzania; and the Kenyan Medical Research Institute. We thank A. Muehlenbachs for assistance in interpreting the electron microscopy images, B. Morrison for assistance with data management, and D. Lanar for the LSA proteins. This work was supported by grants from the U.S. National Institutes of Health (NIH) (grant R01-AI52059) and the Bill & Melinda Gates Foundation (grant 1364) to P.E.D., the Intramural Research Program of the National Institute of Allergy and Infectious Diseases–NIH, and grants from NIH (grant R01-AI076353) and an internal Lifespan Hospital System Research Pilot Award Grant to J.D.K., and grants from NIH to J.D.D. (R01-AI102907 and DP2-AI112219). C.E.N. (grant T32-DA013911) and I.C.M. (grant 1K08AI00997-01A1) were supported by NIH. We also acknowledge research core services provided by the Rhode Island Hospital imaging core (G. Hovanessian) and core services supported by Lifespan/Tufts/Brown Center for Aids Research (P30AI042853) and Center for Biomedical Research Excellence (P20GM103421). The DNA sequence for PfSEA-1 is available in PlasmoDB (www.PlasmoDB.org) as ID no. PF3D7_1021800. The work presented in this manuscript has been submitted in partial support of patent application PCT/US12/67404 filed with the U.S. Patent Office. J.D.K.,

J.F.F., M.F., and P.E.D. designed the study; J.D.K., D.K.R., J.F.F., M.F., and P.E.D. drafted the manuscript; M.F. and P.E.D. conducted the field-based sample and epidemiologic data collection; C.P.N. conducted the differential screening; D.K.R., L.P., A.L., C.E.N., and L.C. performed the in vitro growth assays; D.K.R. and G.J. performed the immunolocalization; D.K.R. performed the gene knockout studies; C.G.D., E.A.M., S.A., and J.D.D. performed the conditional gene knockdown studies; I.C.M. performed the single-nucleotide polymorphism detection; S.P.-T., L.C., and H.-W.W. performed the antibody detection assays; S.P.-T. expressed and purified rPfSEA-1A and rPbSEA-1A; D.K.R., C.E.N., and S.C. performed the vaccination studies; J.F.F., J.D.K., and S.E.H. performed the statistical analyses; and J.D.K., J.F.F., M.F., and P.E.D. supervised the study. The authors declare no competing financial interests.

SUPPLEMENTARY MATERIALS

www.sciencemag.org/content/334/6186/871/suppl/DC1
Materials and Methods
Supplementary Text
Tables S1 and S2
Figs. S1 to S11
References (27–41)

30 October 2013; accepted 25 April 2014
10.1126/science.1254417

DEEP EARTH

HPSTAR
045_2014

Disproportionation of (Mg,Fe)SiO₃ perovskite in Earth's deep lower mantle

Li Zhang,^{1,2*} Yue Meng,³ Wenge Yang,^{1,4} Lin Wang,^{1,4} Wendy L. Mao,^{5,6} Qiao-Shi Zeng,⁵ Jong Seok Jeong,⁷ Andrew J. Wagner,⁷ K. Andre Mkhoyan,⁷ Wenjun Liu,⁸ Ruqing Xu,⁸ Ho-kwang Mao^{1,2}

The mineralogical constitution of the Earth's mantle dictates the geophysical and geochemical properties of this region. Previous models of a perovskite-dominant lower mantle have been built on the assumption that the entire lower mantle down to the top of the D'' layer contains ferromagnesian silicate [(Mg,Fe)SiO₃] with nominally 10 mole percent Fe. On the basis of experiments in laser-heated diamond anvil cells, at pressures of 95 to 101 gigapascals and temperatures of 2200 to 2400 kelvin, we found that such perovskite is unstable; it loses its Fe and disproportionates to a nearly Fe-free MgSiO₃ perovskite phase and an Fe-rich phase with a hexagonal structure. This observation has implications for enigmatic seismic features beyond ~2000 kilometers depth and suggests that the lower mantle may contain previously unidentified major phases.

The conventional view of materials in Earth's lower mantle, which comprises the largest fraction of our planet (>55% by volume), has evolved greatly in the past 10 years. High-pressure-temperature (*P-T*) experiments of the past century suggested that the predominant phase was ferromagnesian silicate [(Mg,Fe)SiO₃] with the orthorhombic perovskite (pv) structure, unchanging over the enormous *P-T* range from the bottom of the transition zone at 670 km depth (24 GPa) to the core-mantle boundary (CMB) at 2900 km (136 GPa). However, laser-heated diamond anvil cell (DAC) technology coupled with x-ray spectroscopy (XRS) and x-ray diffraction (XRD) probes have led to two key discoveries: namely, the phase transition of (Mg,Fe)SiO₃ pv to the

post-perovskite (ppv) structure (*I-3*) near the D'' layer of the lower mantle, and the pressure-induced spin-pairing of the 3*d* electrons in Fe (*4-6*)

¹Center for High Pressure Science and Technology Advanced Research (HPSTAR), Shanghai 201203, China. ²Geophysical Laboratory, Carnegie Institution of Washington (CIW), Washington, DC 20015, USA. ³High Pressure Collaborative Access Team (HPCAT), Geophysical Laboratory, CIW, Argonne, IL 60439, USA. ⁴High Pressure Synergetic Consortium (HPSynC), Geophysical Laboratory, CIW, Argonne, IL 60439, USA. ⁵Geological and Environmental Sciences, Stanford University, Stanford, CA 94305, USA. ⁶Photon Science, SLAC National Accelerator Laboratory, Menlo Park, CA 94025, USA. ⁷Department of Chemical Engineering and Materials Science, University of Minnesota, Minneapolis, MN 55455 USA. ⁸Advanced Photon Source, Argonne National Laboratory, Argonne, IL 60439, USA.

*Corresponding author. E-mail: zhangli@hpstar.ac.cn

that dramatically alters the chemical and physical behavior of the Fe-bearing silicates and oxides (7). These discoveries have triggered a flurry of new theories for the enigmatic seismic and geodynamic features observed in the deep lower mantle, such as the geothermal and seismic signatures of the spin transition in Fe-bearing minerals, the correlations between the pv-ppv P - T boundary and the D'' discontinuity and velocity gradients, and possible mineralogical mechanism for the existence of large low-shear-velocity provinces (LLSVPs) (1, 5, 8–11).

Recent sound-velocity measurements of silicate pv and (Mg,Fe)O ferropericlasite (fp) suggested that the (Mg,Fe)SiO₃ pv-dominant petrological model (12) would be consistent with the density profile of the lower mantle (13). The MgSiO₃-FeSiO₃ pseudo-binary phase relations, however, have only been well investigated at the P - T conditions corresponding to the top half of the lower mantle (14, 15). Beyond 60 GPa, detailed studies of this phase diagram are still scarce and reconnaissance in nature (16–19).

Disproportionation of (Mg,Fe)SiO₃

To more directly interrogate these phase relations, we brought crystalline (Mg_{0.85}Fe_{0.15})SiO₃ (Fs15) orthopyroxene (opx) sample to the pressures (60 to 110 GPa) and temperatures (2000 to 2400 K) of the lower mantle using DAC technology (20). We monitored the growth of crystalline phases with in situ XRD under high P - T laser-heating conditions as well as after T -quench at high P .

Compressing Fs15 to 95 GPa at 300 K, the opx powder XRD peaks broaden substantially, but the sample was not amorphized. Instead, the broad peaks resemble the major peaks of pv (fig. S4), indicating a nanocrystalline pv-like structure. The pattern sharpens with moderate heating at 1500 to 2000 K and forms normal crystalline pv, with unit cell parameters consistent with the 15% Fs composition (fig. S4). Increasing temperature to 2300 K above 95 GPa (fig. S4) or heating directly to this P - T condition (Fig. 1A), the pv-dominated powder XRD pattern exhibited subtle additional features. At 101 GPa, the pv unit cell of $a = 4.362(1)$ Å, $b = 4.611(4)$ Å, $c = 6.343(3)$ Å, and molecular volume $V = 31.89(3)$ Å³ ($Z = 4$) is too small for that expected of (Mg_{0.85}Fe_{0.15})SiO₃ but close to that of the pure endmember MgSiO₃ pv at the same pressure (21). In addition to pv, another set of peaks not corresponding to any previously known phases appeared with particularly conspicuous peaks at 2.55 and 2.40 Å (marked H110 and H101, respectively). These two peaks are close to the diagnostic ppv peaks near 2.5 and 2.4 Å (ppv 022 and 110, respectively), but the high-quality XRD pattern clearly rejects the possibility of ppv. On the basis of three distinct new peaks at 4.413, 2.549, and 2.401 Å and several additional peaks (Tables 1 and 2), we concluded that this phase has a hexagonal unit cell of $a = 5.096(2)$ Å and $c = 2.862(3)$ Å and a molecular volume $V = 32.19(4)$ Å³ with formula units per unit cell $Z = 2$ (Tables 1 and 2), referred to as the “H-phase.” The slightly larger molar volume of the H-phase as compared with the

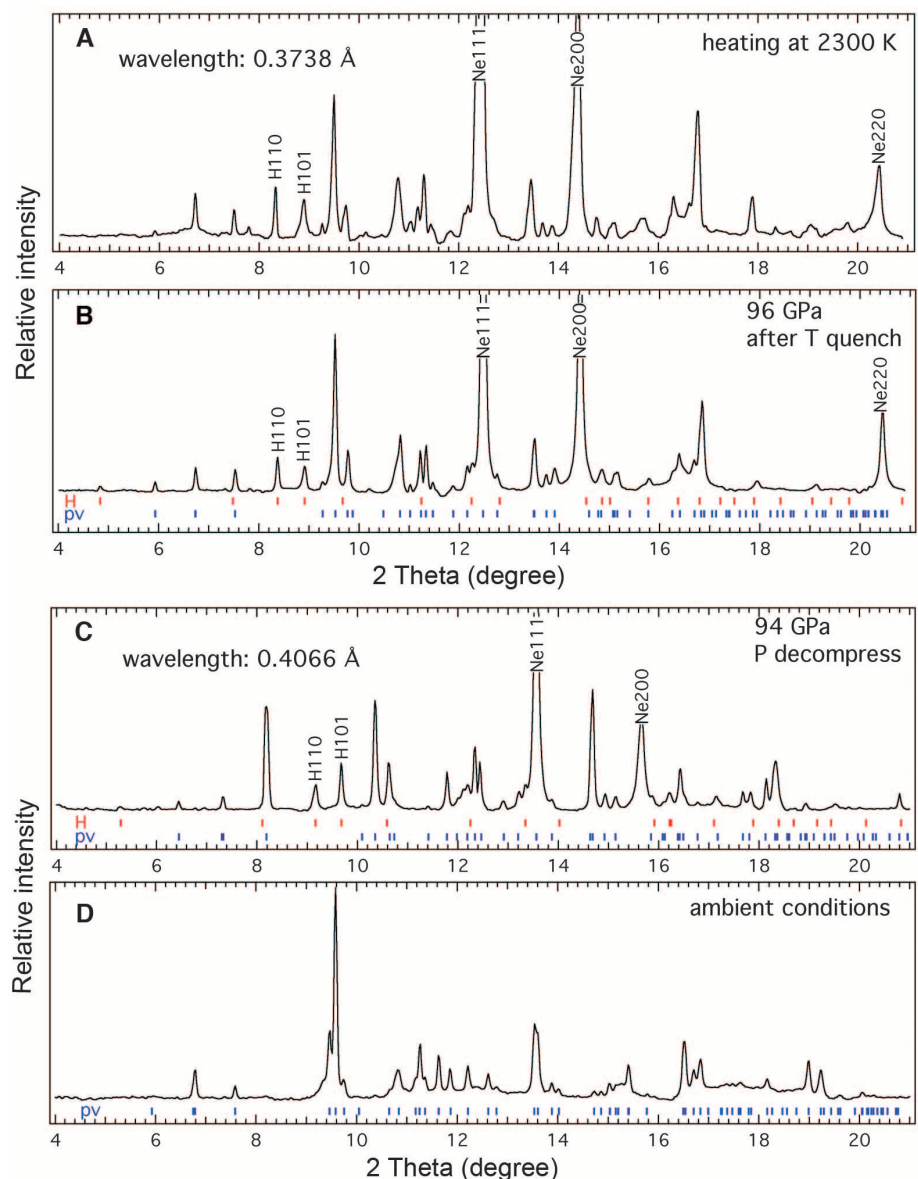


Fig. 1. In situ powder XRD patterns of Fs15 in Ne medium. (A and B) Coexistence of pv phase and H-phase (A) during laser-heating at 2300 K and (B) after T quench to 300 K and 96 GPa. (C and D) Another coexisting pv phase and H-phase decompressed from 101 GPa (C) to 94 GPa at 300 K and then (D) to ambient conditions. Because of the multigrain spotty nature of the patterns, the relative peak intensities are affected by the presence or absence of strong spots. The peak at $d \sim 2.7$ Å, which is 7.8° in (B), belongs to a small amount of SiO₂ (CaCl₂ structure) added to the starting material (20).

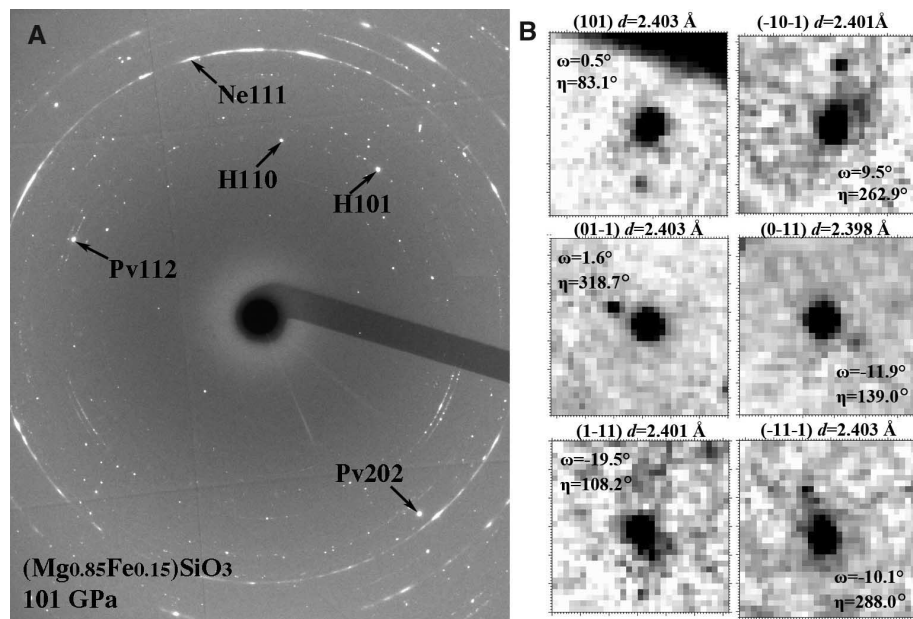
Table 1. Powder XRD data for the H-phase in Fs15 starting composition at 101 GPa. The unit-cell parameters of the H-phase are $a = 5.096(2)$ Å, $c = 2.862(3)$ Å; $\alpha = \beta = 90^\circ$, $\gamma = 120^\circ$ at 101 GPa. The powder XRD pattern was obtained with x-ray wavelength of 0.5164 Å. h , k , l represent Miller indices of reflections; 2θ , Bragg angle; d , d -spacing; obs, observed; calc, calculated; diff, difference.

h	k	l	2θ -obs (degrees)	d -obs (Å)	d -calc (Å)	d -diff (Å)
1	0	0	6.708	4.4133	4.4133	0.0000
1	1	0	11.629	2.5487	2.5480	-0.0007
1	0	1	12.346	2.4012	2.4013	0.0001
1	1	1	15.591	1.9036	1.9031	-0.0005
3	0	0	20.218	1.4710	1.4711	0.0001
2	1	1	20.645	1.4409	1.4411	0.0002

Table 2. Single-crystal XRD data for the H-phase in Fs15 starting composition at 101 GPa.

The unit-cell parameters of the H-phase are $a = 5.096(2)$ Å, $c = 2.862(3)$ Å; $\alpha = \beta = 90^\circ$, $\gamma = 120^\circ$ at 101 GPa. The single-crystal XRD data of one of the crystallites was obtained for the H-phase with an x-ray wavelength of 0.3738 Å. The Bragg angle 2θ , rotation angle ω , and azimuthal angle η are calculated from the orientation matrix and observed as XRD spots.

<i>h</i>	<i>k</i>	<i>l</i>	2θ (degrees)	ω (degrees)	η (degrees)	<i>d</i> (Å)
-1	0	1	8.93	-1.3	63.4	2.395
-1	1	1	8.93	-16.2	32.8	2.395
0	1	-1	8.93	-11.4	268.8	2.401
1	-1	-1	8.95	0.3	212.8	2.399
1	0	-1	8.95	8.7	243.2	2.402
-1	-1	1	11.29	3.0	87.4	1.897
1	1	-1	11.27	14.3	267.3	1.902
-2	2	1	12.3	12.1	22.1	1.741
0	-2	1	12.27	-12.4	105.9	1.746
0	2	-1	12.25	0.3	285.7	1.751
-1	-2	1	14.92	3.9	101.7	1.436
1	0	-2	15.82	-4.1	240.6	1.358
-2	1	2	17.28	-12.4	47.6	1.242
-1	-1	2	17.29	-15.6	75.8	1.242
1	1	-2	17.22	2.3	255.7	1.248
2	-1	-2	17.25	11.0	227.4	1.245
-2	0	2	17.97	-6.5	63.1	1.194
2	-2	-2	17.95	8.6	211.9	1.198
2	0	-2	17.93	13.7	242.9	1.199
-1	4	-1	19.04	0.5	304.4	1.129
-1	-2	2	19.89	-12.1	88.0	1.082
1	2	-2	19.79	7.8	267.9	1.087
2	1	-2	19.81	16.8	256.4	1.086
-3	2	2	19.88	-3.1	38.2	1.081
0	-4	1	20.94	-8.4	120.3	1.029
0	4	-1	20.82	15.6	300.1	1.033
0	3	-2	20.92	0.4	278.7	1.030

**Fig. 2. Selection of MgSiO_3 pv and H-phase individual single crystals using the multigrain method.**

(A) A representative spotty multiple-crystal XRD pattern of the H-phase and coexisting pv in Fs15 at 101 GPa and after T quench (x-ray wavelength of 0.3738 Å), and the marked Miller indices show some of the most intense diffraction spots. (B) Six {101} diffraction reflections at different rotation angle ω and azimuthal angle η belonging to one selected crystallite of the H-phase at 101 GPa.

coexisting MgSiO_3 pv suggests an $(\text{Mg,Fe})\text{SiO}_3$ composition with Fe enrichment.

We repeated the Fs15 experiments with Ne pressure medium five times over the same P - T region and were able to observe the disproportionation reaction and the formation of the H-phase repeatedly (Fig. 1 and fig. S4). We found that the H-phase grows more readily in the Ne medium, which provides a quasi-hydrostatic environment that is superior to that of other media. To eliminate the possibility of any experimental artifacts introduced by Ne, we have also successfully repeated the observation of the disproportionation and appearance of the H-phase with SiO_2 glass as the pressure media and insulation layers without Ne.

Symmetry and Unit Cell Parameters of H-phase

In the two-phase mixed XRD pattern, the low-symmetry orthorhombic pv has many peaks interfering with the H-phase peaks at the low d -spacing region; only three peaks above 2.4 Å are specific to the H-phase. Moreover, powder XRD patterns only contain d -spacing information, and successful indexing of multiple peaks could still be inconclusive. The spottiness of the XRD powder pattern may also introduce uncertainty in peak intensity (fig. S8). On the other hand, single-crystal XRD contains three-dimensional orientation and geometrical relationship in addition to d -spacings and thus provides a more definitive characterization of the unit cell.

We used a multigrain crystallography method (22) to search and determine the orientation matrices of multiple individual crystallites simultaneously within the sample (20). We conducted prolonged laser-heating that promoted growth of a coarser-grained multiple-crystal aggregate, including MgSiO_3 pv and H-phase crystals at 101 GPa (Fig. 2A). By rotating the ω (vertical) axis of the DAC holder to $\pm 21^\circ$ at the steps of 0.1° , 154 individual crystallites—each with 11 to 27 reflections consistent with the H-phase—were identified within the x-ray beam spot of 6 by 8 μm (Tables 1 and 2 and table S1). Six {101} diffraction reflections belonging to three Friedel's pairs from another crystallite further confirm these results (Fig. 2B). With the stringent requirement that all reflections from each of the 154 crystallites must satisfy the d -spacing, rotation angle ω , and azimuthal angle η predicted by its particular orientation matrix, we confirmed the symmetry and the basic unit cell of the H-phase. For comparison in the same sample at 101 GPa using the same indexing procedure (20), we also identified and indexed 130 individual crystallites of the MgSiO_3 pv phase to the known $Pbnm$ space group, with the maximum of 48 reflections observed in a crystallite.

To verify that all predicted reflections were indeed from the same single crystallite and not fortuitously from the diffraction of another crystallite within the 6 by 8 μm x-ray spot, we were able to cover only about 10 crystallites by using the 0.3 by 0.5 μm focused polychromatic and monochromatic x-ray beam (23). The polychromatic Laue XRD spots of different Miller indices appear and disappear

together, indicating that they originate from the same single crystallite. We mapped the relatively large crystallites by using the x-ray beam, monitored the diffraction intensity, and observed that the intensities of the diffraction spots dropped ~50% after moving 0.5 μm in each direction, thus confirming the crystallite size to be typically ~0.5 μm or less (fig. S10).

Fe Depletion in Perovskite

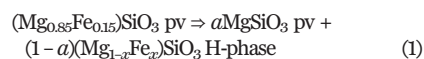
All powder XRD peaks observed at 101 GPa could be assigned to the MgSiO_3 pv phase and H-phase. To confirm that the pv is indeed the MgSiO_3 endmember, we decompressed and monitored the disproportionation product with in situ XRD. The pv phase remains crystalline, with unit cell consistent with the MgSiO_3 pv all the way to ambient pressure (Fig. 1D), and all peaks in the powder XRD pattern can be assigned to the MgSiO_3 pv phase with unit cell parameters $a = 4.784(2)$ \AA , $b = 4.930(2)$ \AA , $c = 6.903(4)$ \AA , and $V = 162.8(1)$ \AA^3 , which is in agreement with the established ambient pv values with $x = 0.02(2)$.

We also performed scanning transmission electron microscopy (STEM) analysis on the recovered sample for phase identification and compositional analysis (20). First, we prepared a thin specimen with focused ion beam (FIB) and mapped it using energy-dispersive x-ray (EDX) to locate the MgSiO_3 region (Fig. 3). The STEM-EDX compositional mapping indicates four regions of distinct compositions marked as positions 1 to 4 on the TEM-bright field (BF) image (Fig. 3A). The selected area electron diffraction (SAED) in position 1 shows the quenched crystalline pv structure (Fig. 3G), and the chemical analysis verified $x = 0.02(2)$ based on multiple analyses (fig. S6); therefore, it can be nominally referred to as MgSiO_3 . The STEM analysis shows that the composition and structure of the quenched pv match the XRD data of the same pv quenched to ambient conditions, confirming the Fe depletion in the pv as a result of the disproportionation. The overall quantity of SiO_2 in the recovered sample (position 2) is consistent with the excess SiO_2 in the starting composition and the in situ XRD observations (Fig. 3H and fig. S6). In contrast to the preservation of the crystalline MgSiO_3 pv, the H-phase was unquenchable and amorphized during decompression; its XRD peaks completely disappeared (Fig. 1D). The amorphous product was highly unstable under ambient conditions and further decomposed during the sample preparation process for STEM (positions 3 and 4). The Fe enrichment in H-phase was confirmed with EDX at ambient conditions (fig. S6), but its unit cell parameters and composition must be characterized in situ at high P . We also tested the reversibility of the disproportionation in the Ne medium by performing heating during decompression and observed that the H-phase clearly diminishes, and only the pv peaks remained at 67 GPa and 2000 K (fig. S7).

Geophysical Implications

The XRD pattern of the disproportionation products only contains the MgSiO_3 pv and H-phase, indicating

that the H-phase has the opx stoichiometry and Fe enrichment ($x > 0.15$), as in the following reaction:



According to the phase rule, at a given P - T condition compositions of both MgSiO_3 pv and the H-phase are fixed in the pseudo-binary system. The best approach to determine the H-phase composition x , therefore, would be to synthesize a pure H-phase in situ. We tested another opx starting

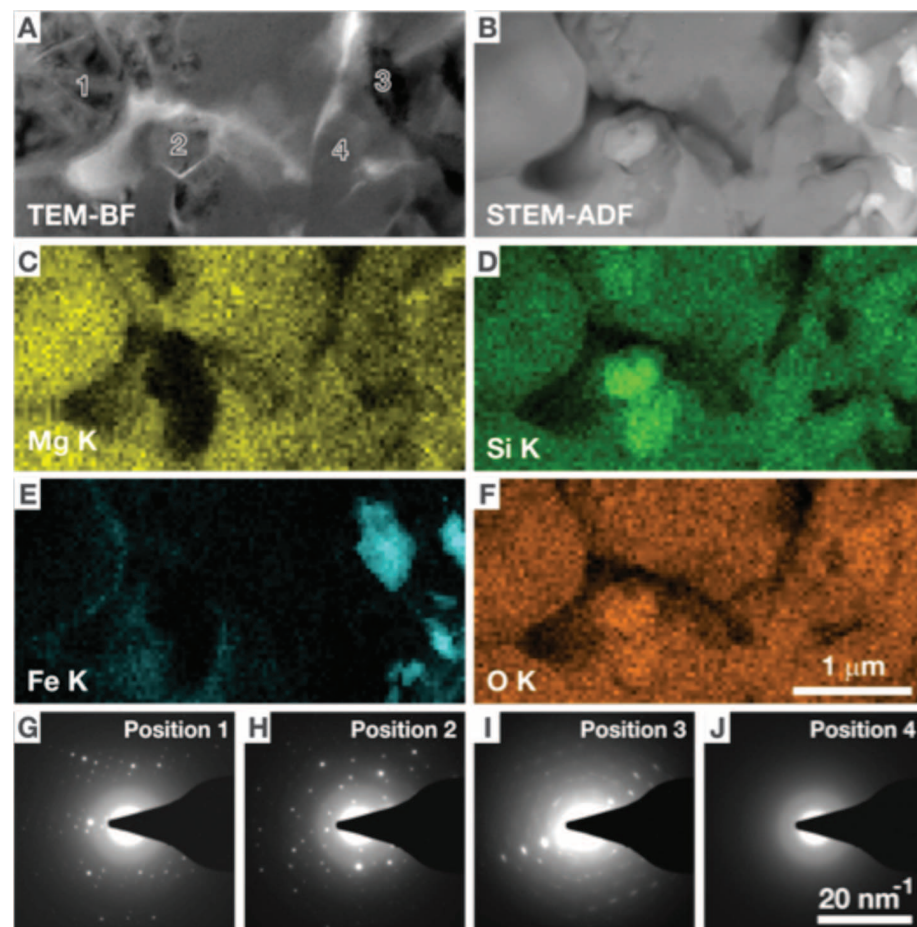


Fig. 3. STEM-EDX analysis of the recovered products. (A) TEM-BF image. (B) STEM-annular dark-field (ADF) image. (C to F) Corresponding STEM-EDX maps: (C) Mg K, (D) Si K, (E) Fe K, and (F) O K. STEM-ADF and EDX maps were obtained simultaneously. (G to J) SAED patterns obtained from the positions indicated in (A).

Table 3. Powder XRD pattern for the H-phase at 85 GPa. The H phase was synthesized in a starting composition $(\text{Mg}_{0.60}\text{Fe}_{0.40})\text{SiO}_3$ (Fs40) and has unit-cell parameters of $a = 5.136(6)$ \AA , $c = 2.883(3)$ \AA (x-ray wavelength: 0.3978 \AA).

<i>h</i>	<i>k</i>	<i>l</i>	2 θ -obs (degrees)	<i>d</i> -obs (\AA)	<i>d</i> -calc (\AA)	<i>d</i> -diff (\AA)
1	0	0	5.124	4.4495	4.4479	-0.0016
1	1	0	8.890	2.5663	2.5680	0.0017
1	0	1	9.434	2.4186	2.4193	0.0007
2	0	0	10.250	2.2266	2.2240	-0.0026
1	1	1	11.934	1.9133	1.9176	0.0043
2	0	1	12.977	1.7601	1.7609	0.0008
2	1	0	13.606	1.6791	1.6812	0.0021
3	0	0	15.413	1.4832	1.4826	-0.0006
2	1	1	15.756	1.4511	1.4523	0.0012
0	0	2	15.863	1.4414	1.4415	0.0001
1	0	2	16.661	1.3728	1.3713	-0.0015
3	0	1	17.340	1.3194	1.3185	-0.0009
2	2	0	17.809	1.2850	1.2840	-0.0010
2	2	1	19.520	1.1733	1.1729	-0.0004

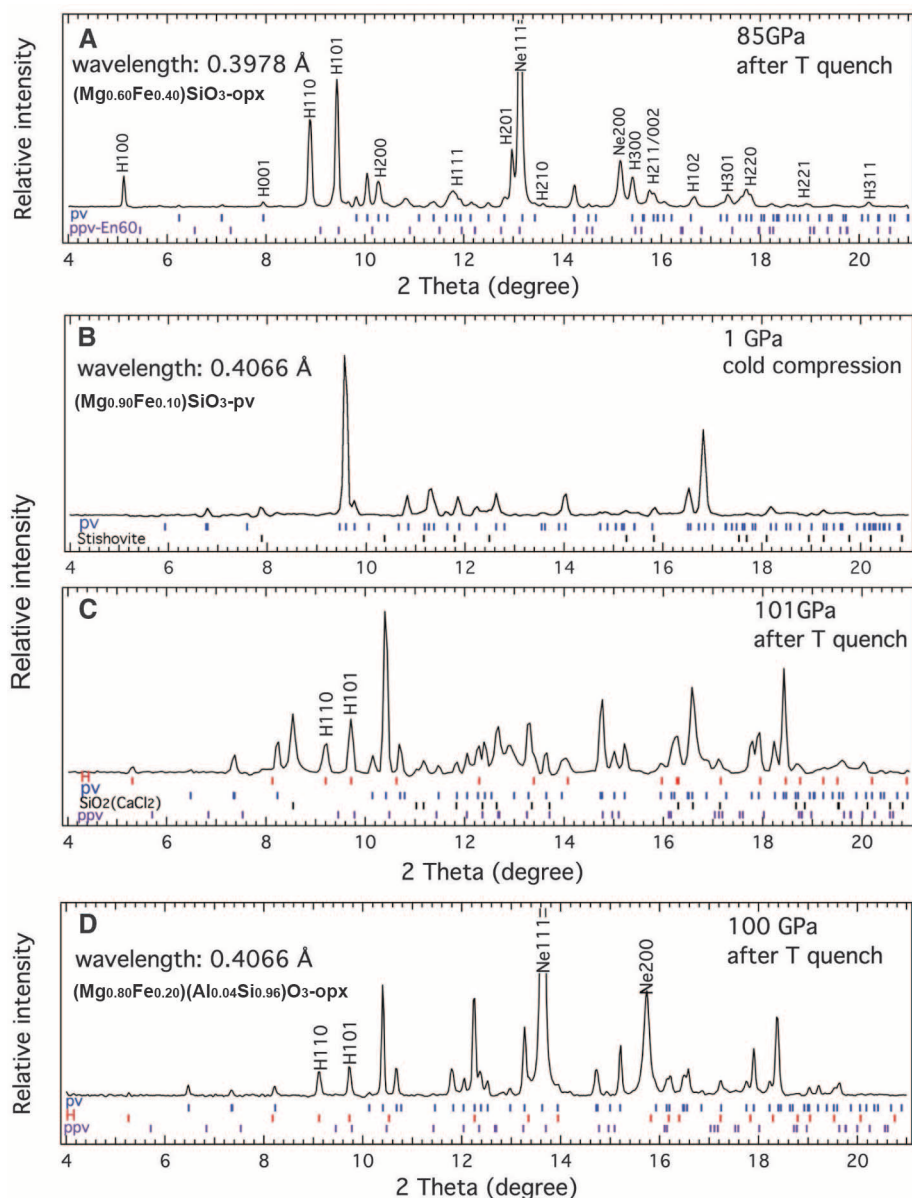


Fig. 4. XRD powder patterns of run products from different starting compositions. **(A)** H-phase-dominant XRD pattern in the Fs40 composition at 85 GPa after *T*-quench to 300 K (Table 3). **(B)** Cold compression of pv10 starting material in SiO₂ glass medium and **(C)** XRD pattern of coexisting pv phase and H-phase after *T*-quench from heating at 2350 to 300 K at 101 GPa. **(D)** XRD pattern of disproportionation products of (Mg_{0.80}Fe_{0.20})(Al_{0.04}Si_{0.96})O₃ opx at 100 GPa after *T*-quench to 300 K from heating at 2300 K. The calculated peak positions of the H, pv, and SiO₂ (CaCl₂ structure) phases are indicated by small ticks, and the calculated peak positions of the ppv phase at the same *P-T* conditions are also shown for comparison.

material with the composition of (Mg_{0.60}Fe_{0.40})SiO₃ (Fs40), compressed it to 60 GPa, and laser heated it to 2100 K. Consistent with the previously known phase relations (15), all observed XRD peaks can be assigned to three coexisting phases: SiO₂, (Mg,Fe)Ofp, and (Mg,Fe)SiO₃ pv; no H-phase was observed. When the Fs40 was directly compressed to 85 GPa and heated to 2300 K, however, we observed a powder XRD pattern consisting of predominately H-phase, with only a minor amount of pv peaks (Fig. 4A), indicating that the H-phase composition is close to (Mg_{0.6}Fe_{0.4})SiO₃. Refinement of 15

powder XRD peaks of the H-phase yields a hexagonal unit cell of $a = 5.136(6)$ Å, $c = 2.883(3)$ Å, and $V = 32.93(5)$ Å³ ($Z = 2$) for the H-phase at 85 GPa (Table 3). The volume reduction of the reaction based on the molar volumes of MgSiO₃ pv and the H-phase on the right hand side and the pv on left side (27) was obtained as $\Delta V = -0.27$ Å³ and $\Delta V/V = -0.2\%$ for the (Mg_{0.6}Fe_{0.4})SiO₃ H-phase. The small, negative ΔV indicates that pressure slightly favors the disproportionation, thermodynamically.

Equation 1 implies that any pv in the composition range of $x = 0.02$ to 0.40 will disproportionate

to MgSiO₃ pv and H-phase at the deep lower mantle conditions. To test this conclusion, we used an (Mg_{0.90}Fe_{0.10})SiO₃ sample presynthesized in the pv form (pv10) with a multianvil press (Fig. 4B). The pv10 starting material is from the same batch that has been used extensively in previous studies and publications (6, 14, 24, 25) and is considered a realistic mineral component for the Earth's interior. Again, we observed the disproportionation to an assemblage of Fe-depleted pv and H-phase (Fig. 4C). The direct transition from the stable phase of pv, rather than from a metastable opx starting material, demonstrates the relative stability. Because we can convert the Fe-bearing pv to coexisting Fe-depleted pv and H-phase, but have not been able to convert H-phase to Fe-bearing pv in this *P-T* range even with extensive heating, we conclude that the disproportionation assemblage is more stable than is Fe-bearing pv.

Most Earth models include excess fp in addition to the major mineral of pv. We conducted an experiment with the starting composition of MgO:FeO:SiO₂ = 0.86:0.19:1.0 (pv:fp = 100:5 or opx:olivine = 95:5). The H-phase was again observed at 97 GPa after laser-heating in the fp-saturated environment, confirming the disproportionation of pv in the MgO-FeO-SiO₂ ternary system (fig. S11). We also consider the trivalent minor components of Al and Fe³⁺, which are coupled according to previous studies (26). We performed another set of experiments using an Al-bearing opx starting material (Mg_{0.80}Fe_{0.20})(Al_{0.04}Si_{0.96})O₃. Again, we observed the robust disproportionation of pv and formation of H-phase (Fig. 4D). The single-crystal data set for one of the H-phase crystallites in the Al-bearing sample confirms these results (table S2).

Both in situ XRD and ex situ STEM-EDX analysis demonstrate the disproportionation reaction of (Mg,Fe)SiO₃ pv to a nearly Fe-free pv and an Fe-rich H-phase at 95 to 101 GPa and 2200 to 2400 K. Therefore, we suggest that (Mg,Fe)SiO₃ pv may not be the major silicate throughout the lower mantle down to the top of the D'' layer. For the lower mantle below 2000 km, all geodynamic models need to consider the physical properties of the Fe-depleted MgSiO₃ pv as a major phase. For instance, the sound-velocity data of MgSiO₃ and MgSiO₃:Al₂O₃ pv (12) can now be applied directly for comparison with seismic data without adjustment for its Fe content. The geochemical importance of high-spin-low-spin transition (4–6) in (Mg,Fe)SiO₃ pv gives way to other Fe-bearing phases, such as oxides or H-phase, in this region. Likewise, interpretations for key enigmatic features in the deep lower mantle—namely, the sharp boundary on the top of the D'' layer, the anticorrelations between V_S and V_P , the seismic anisotropy, and the LLSVPs in the bottom third of the lower mantle (8–11, 27, 28)—may not be limited to the effects of the pv-ppv transition (1–3) but should consider the rich three-phase *P-T-x* relationship of pv, ppv, and the H-phase.

We still do not fully understand the detailed crystal chemistry of the H-phase. For instance,

the atomic positions have not been determined within its unit cell, and the small unit cell that we provided could well be the base for larger superlattices (20). Its composition and phase relation to pv and ppv needs to be determined as a function of *P-T* for interpreting various features in the deep lower mantle. Last, its elasticity and rheological properties are essential for interpretation of deep Earth seismology.

REFERENCES AND NOTES

1. M. Murakami, K. Hirose, K. Kawamura, N. Sata, Y. Ohishi, *Science* **304**, 855–858 (2004).
2. A. R. Oganov, S. Ono, *Nature* **430**, 445–448 (2004).
3. T. Tsuchiya, J. Tsuchiya, K. Umamoto, R. M. Wentzcovitch, *Earth Planet. Sci. Lett.* **224**, 241–248 (2004).
4. J. Badro *et al.*, *Science* **305**, 383–386 (2004).
5. J. Badro *et al.*, *Science* **300**, 789–791 (2003).
6. J. Li *et al.*, *Proc. Natl. Acad. Sci. U.S.A.* **101**, 14027 (2004).
7. S. Stackhouse, *Nat. Geosci.* **1**, 648–650 (2008).
8. E. Ohtani, T. Sakai, *Phys. Earth Planet. Inter.* **170**, 240–247 (2008).
9. R. D. van der Hilst, H. Karason, *Science* **283**, 1885–1888 (1999).
10. E. J. Garnero, A. K. McNamara, *Science* **320**, 626–628 (2008).
11. W. J. Su, R. L. Woodward, A. M. Dziewonski, *J. Geophys. Res.* **99**, 6945 (1994).
12. M. Murakami, Y. Ohishi, N. Hirao, K. Hirose, *Nature* **485**, 90–94 (2012).
13. A. Riccolleau *et al.*, *Geophys. Res. Lett.* **36**, L06302 (2009).

14. Y. Fei, Y. Wang, L. W. Finger, *J. Geophys. Res.* **101**, 11525 (1996).
15. Y. Tange, E. Takahashi, Y. Nishihara, K.-i. Funakoshi, N. Sata, *J. Geophys. Res.* **114**, B02214 (2009).
16. W. L. Mao *et al.*, *Proc. Natl. Acad. Sci. U.S.A.* **102**, 9751–9753 (2005).
17. S. Tateno, K. Hirose, N. Sata, Y. Ohishi, *Phys. Earth Planet. Inter.* **160**, 319–325 (2007).
18. J.-F. Lin *et al.*, *Nat. Geosci.* **1**, 688–691 (2008).
19. S. M. Dorfman, Y. Meng, V. B. Prakapenka, T. S. Duffy, *Earth Planet. Sci. Lett.* **361**, 249–257 (2013).
20. Materials and methods are available as supplementary materials on Science Online.
21. S. Lundin *et al.*, *Phys. Earth Planet. Inter.* **168**, 97–102 (2008).
22. H. O. Sørensen *et al.*, *Z. Kristallogr.* **227**, 63–78 (2012).
23. L. Wang *et al.*, *Proc. Natl. Acad. Sci. U.S.A.* **107**, 6140–6145 (2010).
24. Y. Fei, D. Virgo, B. O. Mysen, Y. Wang, H. K. Mao, *Am. Mineral.* **79**, 826 (1994).
25. J. M. Jackson *et al.*, *Am. Mineral.* **90**, 199–205 (2005).
26. R. Sinmyo, K. Hirose, S. Muto, Y. Ohishi, A. Yasuhara, *J. Geophys. Res.* **116**, B07205 (2011).
27. A. R. Hutko, T. Lay, J. Revenaugh, E. J. Garnero, *Science* **320**, 1070–1074 (2008).
28. M. Panning, B. Romanowicz, *Science* **303**, 351–353 (2004).

ACKNOWLEDGMENTS

We thank Y. Fei for providing the pv10 starting material; J. Shu, M. Somayazulu, E. Rod, G. Shen, S. Sinogeikin, P. Dera, V. Prakapenka, and S. Tkachev for their technical support. We also thank S. Merkel for introducing us to the indexing software. The research is supported by National Science Foundation

(NSF) grants EAR-0911492, EAR-1119504, EAR-1141929, and EAR-1345112. This work was performed at HPCAT (Sector 16), Advanced Photon Source (APS), Argonne National Laboratory. HPCAT operations are supported by the U.S. Department of Energy–National Nuclear Security Administration (DOE–NNSA) under award DE-NA0001974 and DOE–Basic Energy Sciences (BES) under award DE-FG02-99ER45775, with partial instrumentation funding by NSF. HPSynC is supported as part of EFree, an Energy Frontier Research Center funded by DOE–BES under grant DE-SC0001057. Portions of this work were performed at GeoSoilEnviroCARS (sector 13), APS, supported by the NSF–Earth Sciences (EAR-1128799) and DOE–GeoSciences (DE-FG02-94ER14466), at 34ID-E beamline, APS, and at 15U1, Shanghai Synchrotron Radiation Facility. Use of the APS facility was supported by DOE–BES under contract DE-AC02-06CH11357. This work was also partially supported by the Materials Research and Engineering Center program of the NSF under award DMR-0819885. Part of this work was carried out in the Characterization Facility of the University of Minnesota. All other data used to support conclusions in this manuscript are provided in the supplementary materials

SUPPLEMENTARY MATERIALS

www.sciencemag.org/content/344/6186/877/suppl/DC1
Materials and Methods
Supplementary Text
Figs. S1 to S11
Tables S1 and S2
References (29–34)

30 December 2013; accepted 3 April 2014
10.1126/science.1250274

REPORTS

COSMOLOGY

Holographic description of a quantum black hole on a computer

Masanori Hanada,^{1,2,3*} Yoshifumi Hyakutake,⁴ Goro Ishiki,¹ Jun Nishimura^{5,6}

Black holes have been predicted to radiate particles and eventually evaporate, which has led to the information loss paradox and implies that the fundamental laws of quantum mechanics may be violated. Superstring theory, a consistent theory of quantum gravity, provides a possible solution to the paradox if evaporating black holes can actually be described in terms of standard quantum mechanical systems, as conjectured from the theory. Here, we test this conjecture by calculating the mass of a black hole in the corresponding quantum mechanical system numerically. Our results agree well with the prediction from gravity theory, including the leading quantum gravity correction. Our ability to simulate black holes offers the potential to further explore the yet mysterious nature of quantum gravity through well-established quantum mechanics.

In 1974, it was realized that a black hole should radiate particles as a perfect black body due to quantum effects in the surrounding space and that the black hole should eventually evaporate completely (1, 2). This phenomenon, which is known as the Hawking radiation, made more accurate the close analogy between the laws of black hole physics and those of thermodynamics (3), but it also caused a long scientific debate (4, 5) concerning the information-loss paradox (6, 7). Suppose one

throws a book into a black hole. While the black hole evaporates, all we observe is the black-body radiation. Therefore, the information contained in the book is lost forever. This statement sharply conflicts with a basic consequence of the law of quantum mechanics that the information of the initial state should never disappear. Then the question is whether the law of quantum mechanics is violated or the above argument should somehow be modified if full quantum effects of gravity are taken into account.

Superstring theory, a consistent theory of quantum gravity, enabled us to understand the statistical-mechanical origin of the black hole entropy for a special class of stable black holes by counting the microscopic states, which look like the same black hole from a distant observer (8). The paradox still remains, however, because a complete description of an evaporating black hole is yet to be established. A key to resolve the paradox is provided by the gauge-gravity duality (9), which is conjectured in superstring theory. In a particular case, it claims that black holes in gravity theory can be described in terms of gauge theory in one dimension, which is a standard quantum mechanical system without gravity. The conjecture may be viewed as a concrete realization of the holographic principle (10, 11), which states that all of the information inside a black hole should be somehow encoded on its boundary, namely on the so-called event horizon of the black hole. In gauge theory in general, information is conserved during the time evolution as the standard laws of quantum mechanics simply apply. Therefore, it is widely believed that there is no information loss if the conjectured holographic description of a black hole is correct, including full quantum effects of gravity.

¹Yukawa Institute for Theoretical Physics, Kyoto University, Kitashirakawa Oiwakecho, Sakyo-ku, Kyoto 606-8502, Japan.

²The Hakubi Center for Advanced Research, Kyoto University, Yoshida Ushinomiyacho, Sakyo-ku, Kyoto 606-8501, Japan. ³Stanford Institute for Theoretical Physics, Stanford University, Stanford, CA 94305, USA. ⁴College of Science, Ibaraki University, Bunkyo 2-1-1, Mito, Ibaraki 310-8512, Japan. ⁵Theory Center, High Energy Accelerator Research Organization (KEK), 1-1 Oho, Tsukuba, Ibaraki 305-0801, Japan. ⁶Graduate University for Advanced Studies (SOKENDAI), 1-1 Oho, Tsukuba, Ibaraki 305-0801, Japan.

*Corresponding author. E-mail: hanada@yukawa.kyoto-u.ac.jp